IEEE Access
Multidisciplinary | Rapid Review | Open Access Journal

Received June 2, 2020, accepted June 7, 2020, date of publication June 11, 2020, date of current version June 23, 2020.

Digital Object Identifier 10.1109/ACCESS.2020.3001576

Multifunctional Scattering Antenna Array Design for Orbital Angular Momentum Vortex Wave and RCS Reduction

ZAN KUI MENG, YAN SHI, (Senior Member, IEEE), WEN YUE WEI, AND XIANG FAN ZHANG
School of Electronic Engineering, Xidian University, Xi'an 710071, China

Corresponding author: Yan Shi (shiyan@mail.xidian.edu.cn)

This work was supported in part by the National Natural Science Foundation of China under Grant 61771359, and in part by the Natural Science Basic Research Plan in Shaanxi Province under Grant 2018JM6006.

ABSTRACT In this paper, a multifunctional scattering antenna array has been proposed to generate orbital angular momentum (OAM) vortex scattering wave and meanwhile reduce antenna radar cross section (RCS). Theoretical analysis for integration of the RCS reduction and the OAM wave is given, and a circular antenna array composed of a dual polarized microstrip antenna and a tunable connection line network is designed. By adjusting the ON/OFF state of the PIN diodes embedded in the connection line network, the OAM scattering waves with the modes of $l = 1$ and $l = 2$ are independently generated, and accordingly in-band RCS reduction of a circular patch antenna with an increase of the antenna gain over 2 dB is achieved. A multifunctional prototype antenna array is fabricated and measured. Simulated and measured results demonstrate −10dB RCS reduction and the OAM scattering waves with the tunable modes in the frequency band of 9.37∼9.8 GHz.

INDEX TERMS Multifunctional scattering antenna array, orbital angular momentum (OAM), in-band RCS reduction, tunable modes.

I. INTRODUCTION

Orbital angular momentum (OAM) vortex waves characterized by an azimuthal phase dependence of $exp(il\varphi)$, in which φ is the azimuthal angle and l is an integer known as the mode number, have caused tremendous research interests in scientific communities due to its promising ability in wireless communication. Theoretically, the OAM vortex waves have unlimited range of orthogonal eigenstates. When associating the information with these eigenstates, the OAM multiplexing has the potential to increase the channel capacity in the optical range [1], [2] and at RF [3], [4]. Various approaches including antenna array [5], [6], spiral phase plate [7], [8], holographic plate [9], [10] etc., have been developed to generate the OAM vortex waves from microwave to optical frequencies. Besides, the metamaterial/metasurface inspired reconfigurable antennas and arrays have been proposed to design the OAM vortex waves with tunable beams [11], [12] and tunable modes [13]–[16] for dynamic communication environment.

The associate editor coordinating the review of this manuscript and approving it for publication was Kuang Zhang.

On the other hand, a great variety of coexisting applications in communication systems have triggered the demand of highly efficient multifunctional devices. Especially in the safe communication field, for instance low-observable platforms, how to reduce the radar cross section (RCS) characteristic of the antennas mounted on the platform becomes vital. Some metamaterial-based absorbing structures [17]–[20] have been designed to reduce the antenna RCS. By making the equivalent impedance of the absorbing structure equal to the wave impedance in free space, the incoming wave can penetrate into the absorbing structure without reflection. The use of the lossy materials including lossy dielectric material [17], thin conductivity sheet [18], [19] and lumped resistor [20] converts the incoming energy to the heat. However, application of the absorbing structure into the antenna easily results in deterioration of the radiation performance. In addition, some metasurface-based structures have been developed to accomplish low RCS property by redirecting the scattered wave away from the backscatter direction. The chessboard patterned configurations consisting of two metasurface arrays with 180° reflection phase difference have the low RCS characteristic [21], [22]. Except with the reflection phase

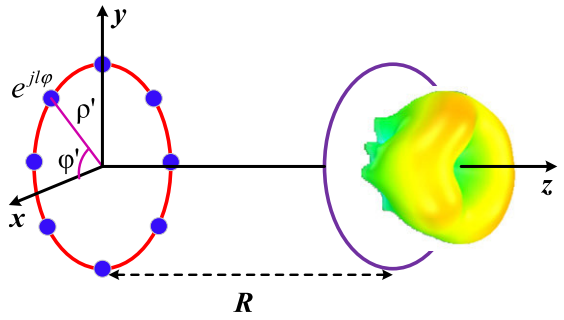

FIGURE 1. Operating mechanism of a multifunctional antenna array.

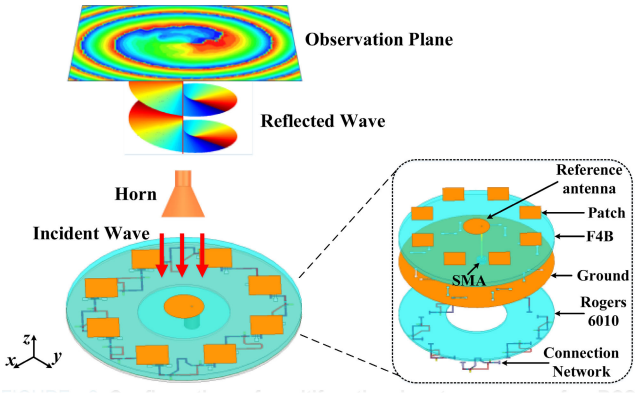

FIGURE 2. Configuration of multifunctional antenna array for RCS reduction and OAM vortex wave.

cancellation based designs, a characteristic mode cancellation method was proposed to achieve the antenna RCS reduction in a wide band [23]. However, a large space is required to arrange the metasurface structures. In order to achieve a compact size, an antenna array based design has been developed to reduce the in-band RCS of the antenna [24] according to the polarization rotation characteristic. However, all reported designs only have a single function of the RCS reduction.

In this paper, a multifunctional antenna array has been designed for the first time to simultaneously generate the OAM vortex scattering wave and reduce antenna RCS. By adjusting ON/OFF state of the PIN diodes in the connection network, the proposed antenna array can convert the incident plane wave to the scattering OAM wave with the modes of $l = 1$ and $l = 2$, respectively, thus achieving an OAM-based communication. Moreover, when the proposed scattering antenna array is integrated with the reference circular antenna, the RCS reduction of the reference antenna can be realized due to the far field property of the OAM wave, which distinguishes the proposed design from previously reported RCS reduction schemes. Simulation and measured results are given to demonstrate the good performance including the scattering OAM wave with tunable modes, the in-band RCS reduction of the reference antenna, and the increase of the reference antenna in the operating band of 9.37∼9.8 GHz.

II. THE PROPOSED OAM WATER ANTENNA DESIGN OF MULTIFUNCTIONAL ANTENNA ARRAY

A. INTEGRATION OF RCS REDUCTION AND OAM WAVE

In order to elaborate the operation mechanism of the integration of the RCS reduction and the OAM wave, consider that the field component $f(\rho', \varphi')$ on the aperture located in xoy plane has the helix phase dependence, as shown in Fig. 1. With a multipole series expansion [25], [26], we have

$$f(\rho', \varphi') = \sum_l f_l(\rho') e^{jl\varphi'}, \tag{1}$$

in which

$$f_l(\rho') = \frac{1}{2\pi} \int_0^{2\pi} f(\rho', \varphi') e^{-jl\varphi'} d\varphi'. \tag{2}$$

The Fourier transform of the $f(\rho', \varphi')$ can be expressed in terms of the radial and azimuth coordinates in the spectral domain k and φ as

$$\begin{aligned} &F(k, \varphi) \\ &= \frac{1}{2\pi} \int_0^{\infty} \int_0^{2\pi} f(\rho', \varphi') e^{-jk\rho' \cos(\varphi - \varphi')} \rho' d\varphi' d\rho' \\ &= \sum_l \frac{1}{2\pi} \int_0^{\infty} \int_0^{2\pi} f_l(\rho') e^{-j[k\rho' \cos(\varphi - \varphi') - l\varphi']} \rho' d\varphi' d\rho'. \end{aligned} \tag{3}$$

Using the integral identity for Bessel functions J_n, i.e.,

$$J_n(k\rho') = \frac{j^n}{2\pi} \int_0^{2\pi} e^{-j(k\rho' \cos\xi - n\xi)} d\xi, \tag{4}$$

(3) can be rewritten as

$$F(k, \varphi) = \sum_l F_l(k) e^{jl\varphi}, \tag{5}$$

where

$$F_l(k) = \frac{1}{j^n} \int_0^{\infty} f_l(\rho') J_l(k\rho') \rho' d\rho'. \tag{6}$$

It can be seen from (5) that the $f_l(\rho')$ and its corresponding spectrum known as far-field power pattern $F_l(k)$ are related by the Hankel transform [25], [26]. Therefore, for any fixed l, the $f_l(\rho')$ determines the $F_l(k)$, and vice versa. For $l \neq 0$, we have $J_l(k\rho') = 0$ at $\rho' = 0$, meaning that the far field has a null amplitude along z direction. Therefore, a helical phase distribution will lead to the RCS reduction in the broadside direction.

B. MULTIFUNCTIONAL ANTENNA ARRAY DESIGN

With the above operation mechanism, a multifunctional scattering antenna array has been developed to simultaneously achieve the OAM vortex wave and the RCS reduction, as shown in Fig. 2. The multifunctional antenna array is composed of a circular antenna array and a connection line network. The circular array consists of a dual polarized microstrip antenna fabricated on two substrates, as shown in Fig. 3. The bottom substrate is Rogers 6010 with relative permittivity of 10.2 and loss tangent of 0.0023, and the top one is F4B with relative permittivity of 2.2 and loss tangent

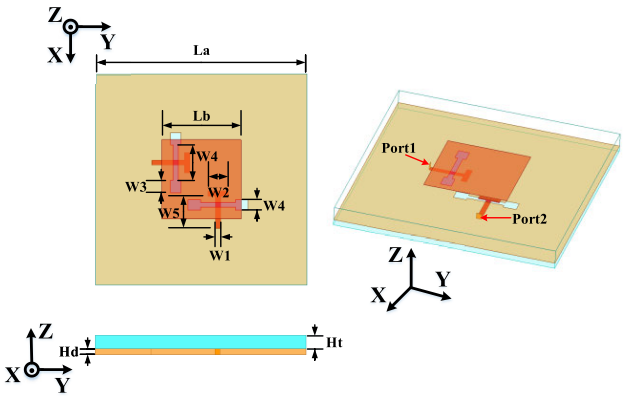

FIGURE 3. Dual polarized antenna element.

TABLE 1. Parameters of the antenna element (unit: mm).

La	21	Lb	9
Ht	1.5	Hd	0.635
W1	0.55	W2	2.3
W3	1.4	W4	1.2
W5	3.7		

of 0.001. The square patch is fabricated on the top substrate and the feeding line is fabricated on the bottom one. The metallic ground with two orthogonally placed I-shaped slots is located between two substrates. A stub is placed at the end of the feeding line for impedance matching. With two orthogonal ports, the proposed microstrip antenna can radiate EM waves with two orthogonal polarizations. The parameters of the antenna element are listed in Table 1. The S parameters and the radiation pattern at 9.6 GHz are given in Fig. 4. The operating band of the antenna element for $S_{11} \leq -10$ dB is 9.36∼9.95 GHz. The realized gain of the element is 7.45 dBi and the 3dB beamwidths in XOZ and YOZ planes cover $-37° \sim 41°$ at 9.6 GHz.

The antenna element is arranged into a circular array, as shown in Fig. 5(a). The dimensions of the array are given in Table 2. The connection line network with PIN diodes (MA4GP907 from Macom) and DC bias circuit including the RF choking inductor of 3.9 nH (LQW15AN from Murata) and DC blocking capacitor of 30 pF (GRM1555C from Murata), is used to connect the antenna elements, as shown in Fig. 5 (b). Each line connects one polarization port of an antenna to the orthogonal polarization port of its adjacent antenna. When a plane wave is incident, a wave with an orthogonal polarization is scattered by the proposed scattering array. Hence the proposed array has polarization rotation characteristic. Moreover, except with the line m1 of 0.99 λg (11.88 mm), each line has two lengths, i.e., mk and mk' (k = 2∼8), which are selectively controlled by four PIN diodes. For instance, the line m2 has the length of 1.12 λg

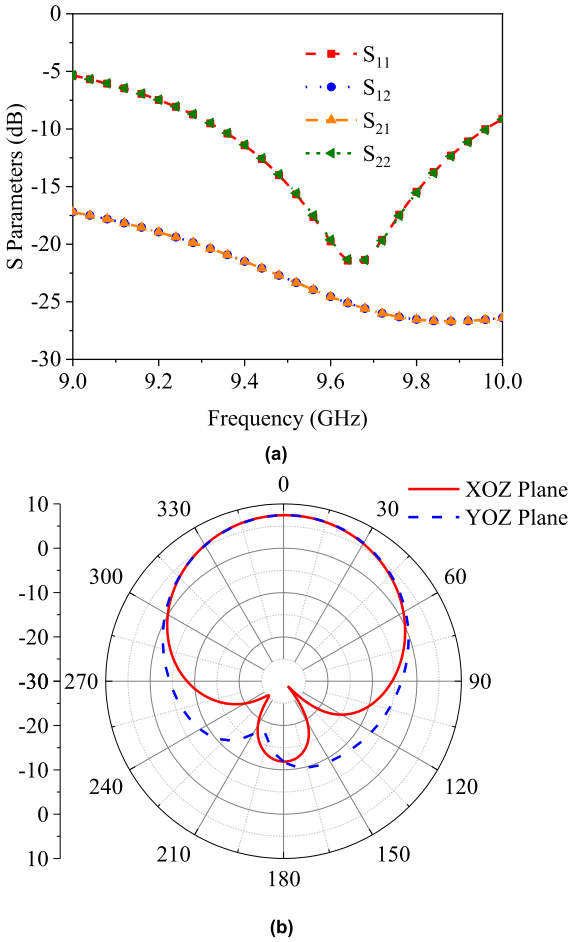

FIGURE 4. S parameters and pattern of the antenna element. (a) S parameters. (b) Pattern.

(13.37 mm) when the PIN diodes 1 and 2 are in ON states and the PIN diodes 3 and 4 are in OFF states, which is called State I. Here λg = 11.99 mm is wavelength in dielectric at 9.6 GHz. In the State I, the length difference between the m2 and the m1 is 0.13 λg, resulting in an approximate phase difference of 45°. With continuously changing the lengths of the mk, a 2π phase distribution along the azimuthal direction can be achieved. Note that the m3 has a length of 1.77 λg (21.23 mm). The length difference between the m3 and the m1 leads to a phase difference of about 270°. Compared with the m1, the layout of the m3 used to connect the antenna ports results in a phase of −180°. Hence the total phase difference between the m3 and the m1 becomes 90°. Similar case holds for the m7. When the PIN diodes 1 and 2 are in OFF states and the PIN diodes 3 and 4 are in ON states, which is called State II, the line m2' has the length of 1.3 λg (15.54 mm), which results in an approximate phase difference of 90° between the m2' and the m1. A phase distribution of 720° is obtained along the azimuthal direction by continuously adjusting the lengths of the mk'. The length of each line is listed in Table 3, and the corresponding operating states are given in Table 4.

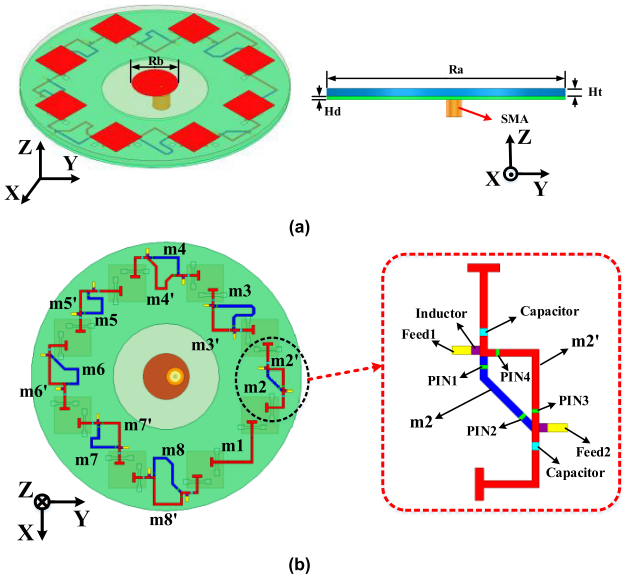

FIGURE 5. The circular array with connection line network. (a) 3D view and side view of the array. (b) Connection line network.

TABLE 2. Parameters of the array (unit: mm).

Ra	66	Rb	11.3
Hd	0.635	Ht	1.5

TABLE 3. Parameters of the connection line network (λ_g = 11.99 mm).

No.	Length/mm	λ_g	No.	Length/mm	λ_g
m1	11.88	0.99	m2/m2'	13.37/15.54	1.12/1.3
m3/m3'	21.23/11.88	1.77/0.99	m4/m4'	17.09/21.22	1.43/1.77
m5/m5'	18.76/11.88	1.56/0.99	m6/m6'	17.01/15.54	1.42/1.3
m7/m7'	15.77/11.88	1.32/0.99	m8/m8'	22.97/21.44	1.92/1.79

TABLE 4. States for the antenna array.

State	PIN 1	PIN 2	PIN3	PIN4	Mode
State I	ON	ON	OFF	OFF	*l*=1
State II	OFF	OFF	ON	ON	*l*=2

The finite-element method (FEM) based solver has been implemented for full-wave simulation of the proposed scattering antenna array. Fig. 6 shows the magnitude and phase of S_{21} of each line in the States I and II. In the two states, the magnitudes of the S_{21} are better than −1 dB in the frequency band from 9 GHz to 10 GHz, which means small transmission loss of each connection line. Phase differences between two adjacent lines in the frequency band of 9∼10 GHz are about 45° and 90°, respectively, in States I and II. In this scenario, when an *x*-polarization plane wave illuminates the proposed array, a *y*-polarization wave with a

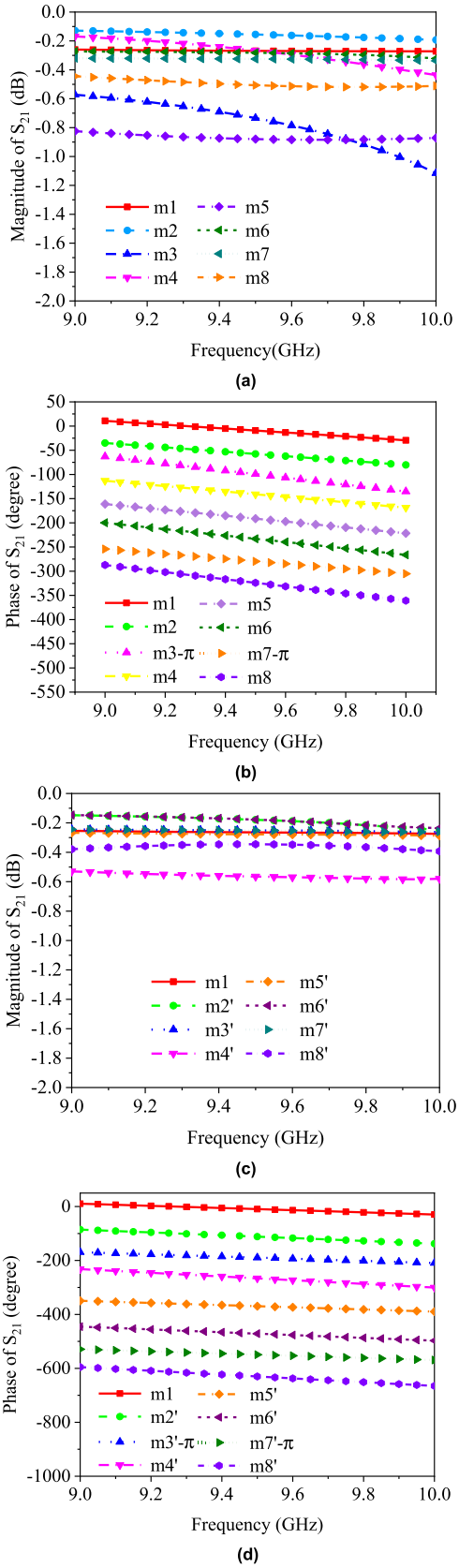

FIGURE 6. S parameters of the connection lines in the network. (a) Magnitude of S_{21} in State I. (b) Phase of S_{21} in State I. (c) Magnitude of S_{21} in State II. (d) Phase of S_{21} in State II.

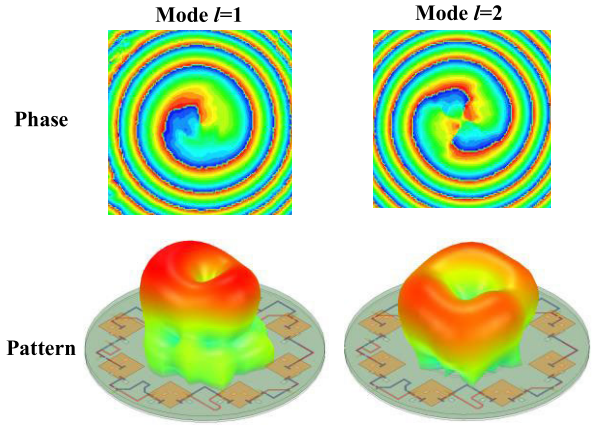

FIGURE 7. Simulated phase distribution of cross-polarized electric field on the observation plane and 3D scattering field in far region at 9.6 GHz.

helix phase is scattered, and thus the OAM scattering wave with the modes of $l = 1$ and $l = 2$ are generated in States I and II, respectively. Fig. 7 shows the phase distribution of the y-polarized scattering field on the observation plane at $z = 288$mm at 9.6 GHz, when a x-polarized horn antenna at $z = 135$ mm is used as a feed source to illuminate the proposed structure. Here the size of the observation plane is chosen as 600 mm$\times$600 mm. We can clearly observe the phase distributions of the OAM scattering wave with the modes of $l = 1$ and $l = 2$. Similar conclusion holds for the y-polarization incident case due to the symmetry of the dual-polarized element. Furthermore, for the circular polarized incident wave, the circular polarized scattering wave carrying the OAM can also be generated. The 3D scattering fields in far region at 9.6 GHz are also shown in Fig. 7. A null amplitude of the electric field along z direction is observed in the two states, which can be used for the RCS reduction. Fig. 8 demonstrates the mode purity of the OAM scattering wave for x-polarized incident wave in a band from 9.3 GHz to 9.9 GHz. Here the y-polarized scattering field is sampled on the circle with a radius of 200 mm on the observation plane. The mode purities better than 86% in the two states are obtained.

On the other hand, the generation of the OAM scattering wave can result in the RCS reduction. Hence the proposed scattering antenna array is integrated with a circular microstrip antenna which is called the reference antenna to reduce the RCS of the reference antenna. The circular patch of the reference antenna is fabricated on the top substrate and fed by a coaxial line. As shown in Fig. 9(a), the operating band of the sole reference antenna for $S_{11} \leq -10$ dB covers 9.36$\sim$9.9 GHz. With the proposed scattering antenna array operating in the States 1 and 2, the frequency band of the reference antenna nearly keeps unchanged. Figs. 9(b) and (c) give the radiation patterns at 9.6 GHz in XOZ and YOZ planes, respectively, when the proposed array is integrated with the reference antenna. It can be found that when the proposed array operates in the two states, the beamwidth of the reference antenna becomes narrow, and thus its gain is

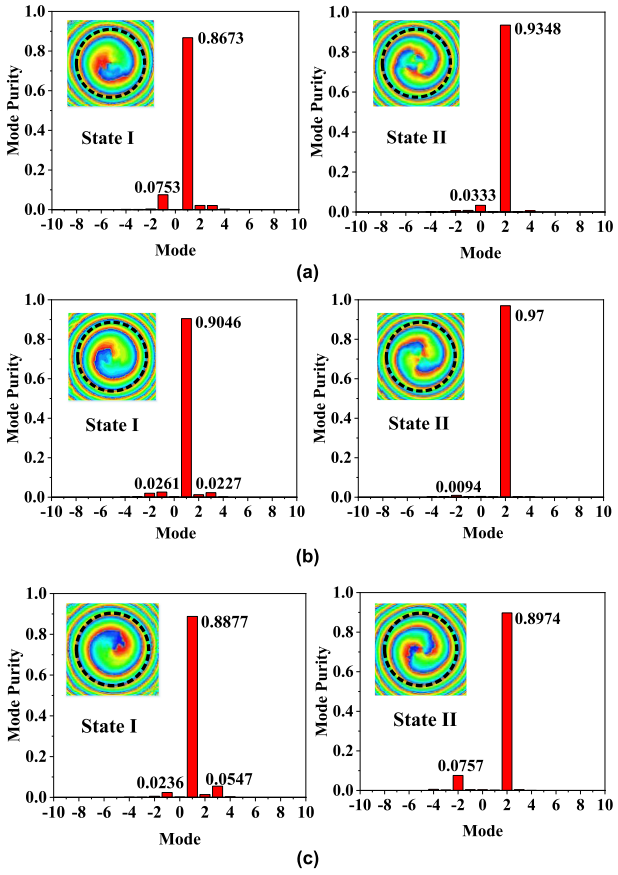

FIGURE 8. Mode purity of the OAM scattering wave in two states. (a) 9.3 GHz. (b) 9.6 GHz. (c) 9.9 GH.

increased. This is because the backward radiation caused by the surface wave of the reference antenna is suppressed by the proposed array. The realized gain of the reference antenna is increased by over 2 dB and 3 dB in the operating band of 9.36 $\sim$9.9 GHz when the proposed antenna array operates

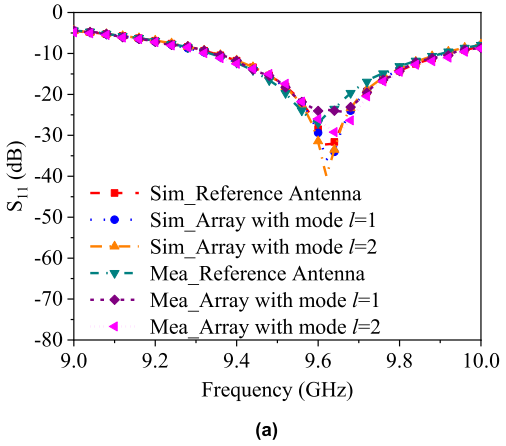

FIGURE 9. Radiation performance comparison between the reference antenna with and without the proposed array. (a) S_{11}. (b) Pattern at 9.6 GHz in XOZ plane. (c) Pattern at 9.6 GHz in YOZ plane. (d) Realized gain.

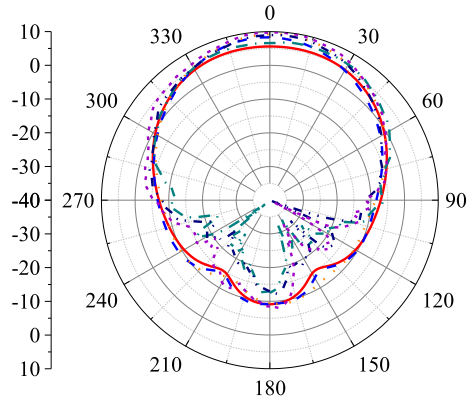

(b)

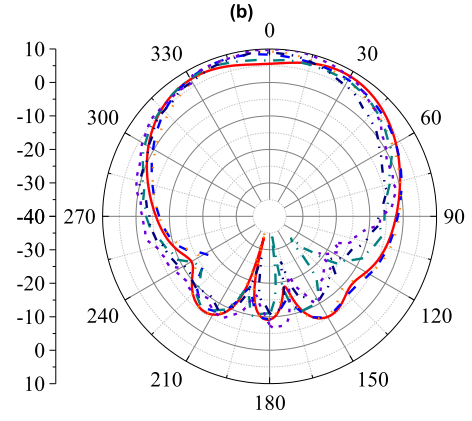

(c)

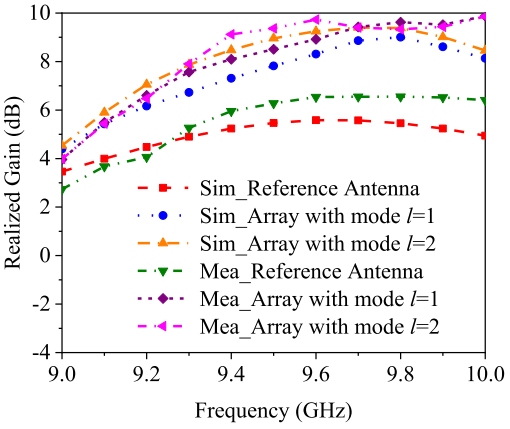

(d)

FIGURE 9. *(Continued.)* **Radiation performance comparison between the reference antenna with and without the proposed array. (a) S_{11}. (b) Pattern at 9.6 GHz in XOZ plane. (c) Pattern at 9.6 GHz in YOZ plane. (d) Realized gain.**

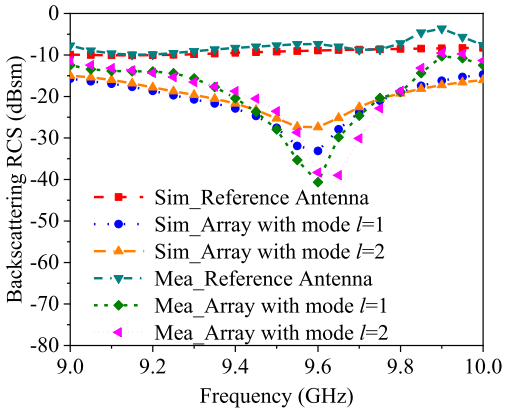

(a)

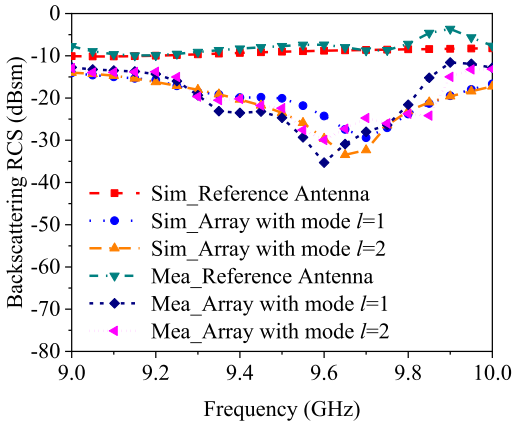

(b)

FIGURE 10. Backscattering performance comparison between the reference antenna with and without the proposed array. (a) XOZ plane. (b) YOZ plane.

in the States I and II, respectively, as shown in Fig. 9(d). At 9.6 GHz, the realized gain increases from 5.58 dB to 8.31 dB and 9.25 dB in the States I and II, respectively.

Fig. 10 depicts the backscattering RCS comparison between the reference antenna with and without the proposed scattering array. It can be seen that −10dB RCS reduction bandwidths in the States I and II cover 9.25∼9.8 GHz and 9.3∼9.85 GHz, respectively in XOZ plane and 9.35∼9.92 GHz and 9.35∼9.95 GHz, respectively in YOZ plane. The in-band RCS reduction of the reference antenna is achieved owing to the OAM scattering waves generated by the proposed scattering antenna array.

III. MEASUREMNTS AND DISSCUSIONS

The proposed multifunctional scattering array integrated with the reference antenna is fabricated and measured, as shown in Fig. 11. Two 1.5-V lithium batteries are applied for the PIN diodes at the Feed 1 and Feed 2 of the connection network shown in Fig. 5(b). The S_{11}, the radiation patterns at 9.6 GHz, and the gain of the reference antennas with and without the proposed scattering array are measured and compared

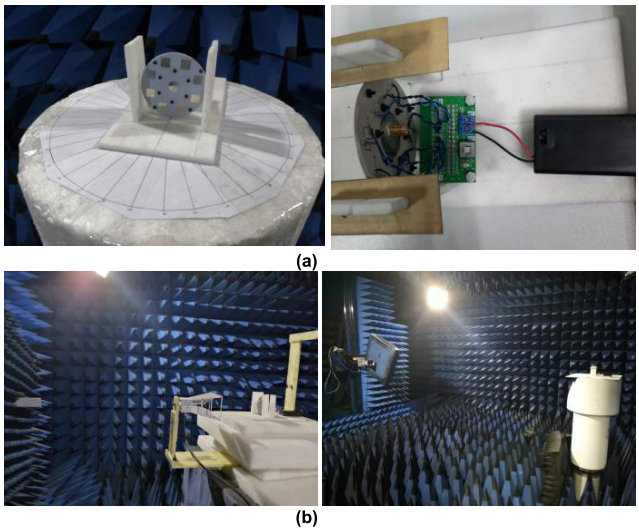

FIGURE 11. Photographs of the fabricated antenna array and the measurement environments. (a) Front view and back view. (b) Near field scanning and RCS measurement.

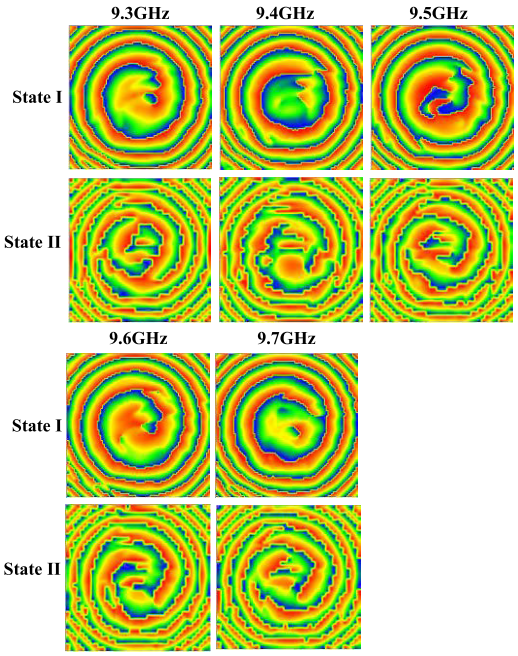

FIGURE 12. The measured phase distributions of the scattering wave on the observation plane at different frequencies.

with the simulation ones, in good agreement between each other, as shown in Fig. 9. The measured impedance band for $S_{11} < -10$ dB in both States I and II covers 9.34∼9.92 GHz. With the proposed array, the realized gain of the reference antenna increases by more than 2.1 dB in the operating band. At 9.6 GHz, the realized gains of the reference antenna without and with the proposed scattering array operating in the two states are 6.5 dBi, 8.9 dBi, and 9.7 dBi, respectively.

The scattering field measurement method for the RCS and the near field planar scanning technique for the OAM vortex wave were performed, respectively. In RCS measurement, two standard horn antennas are used as transmitting and receiving antennas at $z = 2.67$ m in the front of the proposed multifunctional array in the anechoic chamber. As shown in 10, the measured RCSs of the reference antennas with and without the proposed scattering array in XOZ and YOZ planes are in good agreement with simulated ones. The overlapped measurement band for −10dB RCS reduction in the States I and II is 9.37∼9.8 GHz, achieving the in-band RCS reduction of the reference antenna.

In the OAM measurement, a standard horn antenna is placed at $z = 175$ mm in front of the proposed multifunctional array, and a probe with an orthogonal polarization at the observation plane of $z = 400$ mm samples the phase of the electric field in a sampling space of 0.4 mm. Here the overall size of the observation plane is chosen as 0.8 m×0.8 m. Fig. 12 gives the measured phase distributions of the y-polarized scattering wave on the observation plane at $z = 288$mm in the States I and II, when a x-polarized wave is incident. It can be clearly observed that the OAM scattering waves with the modes of $l = 1$ and $l = 2$ are generated in the operating band.

IV. CONCLUSION

In this paper, a multifunctional scattering antenna array has been presented. The design concept is based on the theoretical analysis that the far field of the OAM vortex wave has a null amplitude along broadside direction. By designing a dual-polarized patch element and arranging it into a circular array with a reconfigurable connection line network, the OAM scattering waves with the tunable modes are generated and in-band low RCS characteristic of the reference antenna is obtained. Good agreement between the measurement results and the simulation results verifies the proposed design, which provides a feasible way for the OAM wave based safe communication.

REFERENCES

[1] J. Wang, J.-Y. Yang, I. M. Fazal, N. Ahmed, Y. Yan, H. Huang, Y. Ren, Y. Yue, S. Dolinar, M. Tur, and A. E. Willner, "Terabit free-space data transmission employing orbital angular momentum multiplexing," *Nature Photon.*, vol. 6, no. 7, pp. 488–496, Jul. 2012.

[2] N. Bozinovic, Y. Yue, Y. Ren, M. Tur, P. Kristensen, H. Huang, A. E. Willner, and S. Ramachandran, "Terabit-scale orbital angular momentum mode division multiplexing in fibers," *Science*, vol. 340, no. 6140, pp. 1545–1548, Jun. 2013.

[3] F. Tamburini, E. Mari, A. Sponselli, B. Thidé, A. Bianchini, and F. Romanato, "Encoding many channels on the same frequency through radio vorticity: First experimental test," *New J. Phys.*, vol. 14, no. 3, Mar. 2012, Art. no. 033001.

[4] Y. Yan, G. Xie, M. P. J. Lavery, H. Huang, N. Ahmed, C. Bao, Y. Ren, Y. Cao, L. Li, Z. Zhao, A. F. Molisch, M. Tur, M. J. Padgett, and A. E. Willner, "High-capacity millimetre-wave communications with orbital angular momentum multiplexing," *Nature Commun.*, vol. 5, no. 1, p. 4876, Dec. 2014.

[5] B. Thidé, H. Then, J. Sjöholm, K. Palmer, J. Bergman, T. D. Carozzi, Y. N. Istomin, N. H. Ibragimov, and R. Khamitova, "Utilization of photon orbital angular momentum in the low-frequency radio domain," *Phys. Rev. Lett.*, vol. 99, no. 8, Aug. 2007, Art. no. 087701.

[6] S. M. Mohammadi, L. K. S. Daldorff, J. E. S. Bergman, R. L. Karlsson, B. Thide, K. Forozesh, T. D. Carozzi, and B. Isham, "Orbital angular momentum in radio—A system study," *IEEE Trans. Antennas Propag.*, vol. 58, no. 2, pp. 565–572, Feb. 2010.

[7] M. W. Beijersbergen, R. P. C. Coerwinkel, M. Kristensen, and J. P. Woerdman, "Helical-wavefront laser beams produced with a spiral phase plate," *Opt. Commun.*, vol. 112, nos. 5–6, pp. 321–327, 1994.
[8] M. Uchida and A. Tonomura, "Generation of electron beams carrying orbital angular momentum," *Nature*, vol. 464, no. 7289, pp. 737–739, Apr. 2010.
[9] M. S. Soskin, V. N. Gorshkov, M. V. Vasnetsov, J. T. Malos, and N. R. Heckenberg, "Topological charge and angular momentum of light beams carrying optical vortices," *Phys. Rev. A, Gen. Phys.*, vol. 56, p. 4064, Nov. 1997.
[10] H. Ren, G. Briere, X. Fang, P. Ni, R. Sawant, S. Héron, S. Chenot, S. Vézian, B. Damilano, V. Brändli, S. A. Maier, and P. Genevet, "Metasurface orbital angular momentum holography," *Nature Commun.*, vol. 10, no. 1, p. 2986, Dec. 2019.
[11] S. Yu, L. Li, G. Shi, C. Zhu, X. Zhou, and Y. Shi, "Design, fabrication, and measurement of reflective metasurface for orbital angular momentum vortex wave in radio frequency domain," *Appl. Phys. Lett.*, vol. 108, no. 12, 2016, Art. no. 121904.
[12] D. Zhang, X. Y. Cao, H. H. Yang, J. Gao, and X. W. Zhu, "Multiple OAM vortex beams generation using 1-bit metasurface," *Opt. Express*, vol. 26, no. 19, pp. 24804–24815, 2018.
[13] Y. Shi and Y. Zhang, "Generation of wideband tunable orbital angular momentum vortex waves using graphene metamaterial reflectarray," *IEEE Access*, vol. 6, pp. 5341–5347, 2018.
[14] Z. K. Meng, Y. Shi, W. Y. Wei, Y. Zhang, and L. Li, "Graphene-based metamaterial transmitarray antenna design for the generation of tunable orbital angular momentum vortex electromagnetic waves," *Opt. Mater. Express*, vol. 9, no. 9, pp. 3709–3716, 2019.
[15] J. Ming and Y. Shi, "A mode reconfigurable orbital angular momentum water antenna," *IEEE Access*, vol. 8, pp. 89152–89160, 2020, doi: 10.1109/ACCESS.2020.2993490.
[16] L. Li and X. Zhou, "Mechanically reconfigurable single-arm spiral antenna array for generation of broadband circularly polarized orbital angular momentum vortex waves," *Sci. Rep.*, vol. 8, no. 1, p. 5128, Dec. 2018.
[17] N. I. Landy, S. Sajuyigbe, J. J. Mock, D. R. Smith, and W. J. Padilla, "Perfect metamaterial absorber," *Phys. Rev. Lett.*, vol. 100, no. 20, May 2008, Art. no. 207402.
[18] Y. Zhang, Y. Shi, and C. H. Liang, "Broadband tunable graphene-based metamaterial absorber," *Opt. Mater. Express*, vol. 6, no. 9, pp. 3036–3044, 2016.
[19] L. Zhang, Y. Shi, J. X. Yang, X. Zhang, and L. Li, "Broadband transparent absorber based on indium tin oxide-polyethylene terephthalate film," *IEEE Access*, vol. 7, pp. 137848–137855, 2019.
[20] Y. Shi, Y. C. Li, T. Hao, L. Li, and C.-H. Liang, "A design of ultra-broadband metamaterial absorber," *Waves Random Complex Media*, vol. 27, no. 2, pp. 381–391, Apr. 2017.
[21] Y. Zheng, J. Gao, X. Cao, Z. Yuan, and H. Yang, "Wideband RCS reduction of a microstrip antenna using artificial magnetic conductor structures," *IEEE Antennas Wireless Propag. Lett.*, vol. 14, pp. 1582–1585, 2015.
[22] A. Y. Modi, C. A. Balanis, C. R. Birtcher, and H. N. Shaman, "Novel design of ultrabroadband radar cross section reduction surfaces using artificial magnetic conductors," *IEEE Trans. Antennas Propag.*, vol. 65, no. 10, pp. 5406–5417, Oct. 2017.
[23] Y. Shi, Z. K. Meng, W. Y. Wei, W. Zheng, and L. Li, "Characteristic mode cancellation method and its application for antenna RCS reduction," *IEEE Antennas Wireless Propag. Lett.*, vol. 18, no. 9, pp. 1784–1788, Sep. 2019.
[24] Y. Shi, X. F. Zhang, Z. K. Meng, and L. Li, "Design of low-RCS antenna using antenna array," *IEEE Trans. Antennas Propag.*, vol. 67, no. 10, pp. 6484–6493, Oct. 2019.
[25] A. F. Morabito, L. Di Donato, and T. Isernia, "Orbital angular momentum antennas: Understanding actual possibilities through the aperture antennas theory," *IEEE Antennas Propag. Mag.*, vol. 60, no. 2, pp. 59–67, Apr. 2018.
[26] R. Piessens, "The Hankel transform," in *The Transforms and Applications Handbook*, A. D. Poularikas, Ed. Boca Raton, FL, USA: CRC Press, 2000.

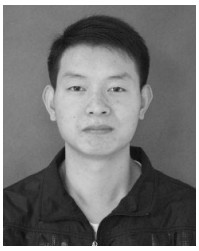

ZAN KUI MENG received the B.E. degree in electronic and information engineering from the North China Institute of Aerospace Engineering, Hebei, China, in 2017. He is currently pursuing the Ph.D. degree in electromagnetics and microwave technology with Xidian University, Xi'an, China. His research interests include Van Atta antenna array design, microwave circuit design, and metamaterial.

YAN SHI (Senior Member, IEEE) received the B.Eng. and Ph.D. degrees in electromagnetic fields and microwave technology from Xidian University, Xi'an, China, in 2001 and 2005, respectively.

He joined the School of Electronic Engineering, Xidian University, in 2005, where he was was promoted to a Full Professor, in 2011. From July 2007 to July 2008, he worked with the City University of Hong Kong, Hong Kong, as a Senior Research Associate. From September 2009 to September 2010, he was a Visiting Postdoctoral Research Associate with the University of Illinois at Urbana–Champaign. From June 2017 to July 2017, he was a Visiting Professor with the State Key Laboratory of Millimeter Wave, City University of Hong Kong. He has authored or coauthored over 100 articles in refereed journal, a book, and a chapter. His research interests include computational electromagnetics, metamaterial, antenna, and wireless power transfer.

Dr. Shi is a Senior Member of the Chinese Institute of Electronics (CIE). He received the Program for New Century Excellent Talents in University awarded by the Ministry of Education of China, in 2011; the New Scientific and Technological Star of Shaanxi Province awarded by the Education Department of Shaanxi Provincial Government, in 2013, the First Prize of Awards for Scientific Research Results of High Education of Shaanxi Province awarded by the Education Department of Shaanxi Provincial Government, in 2013, and Second Prize of Awards of Science and Technology awarded by Shaanxi Province Government in 2015.

WEN YUE WEI received the B.E. degree in electronic and information engineering from Xidian University, Xi'an, China, in 2018, where he is currently pursuing the Ph.D. degree in electromagnetics and microwave technology. His research interests include Van Atta antenna array design, RCS reduction technique, and metamaterial.

XIANG FAN ZHANG received the B.E. degree in electronic and information engineering and the master's degree in electromagnetics and microwave technology from Xidian University, Xi'an, China, in 2016 and 2019, respectively. She is currently an Engineer at Huawei Technologies Company, Ltd. Her research interests include antenna design and metamaterial.